Unveiling dark structures with accurate weak lensing

Herbonnet, R.T.L.; Herbonnet R.T.L.

4

Multi Epoch Nearby Cluster Survey: Weak lensing masses for 48 local galaxy clusters

Large surveys have detected significant samples of galaxy clusters with well-understood selection functions. These can be used to constrain cosmological parameters, provided that their masses can be measured robustly. To extend the calibration of cluster masses using weak gravitational lensing we present results for 48 clusters with $0.05 < z < 0.15$, observed as part of the Multi Epoch Nearby Cluster Survey (MENeaCS). Our measurements benefit from the low cluster redshifts, which decrease contamination of the source sample by cluster members and reduce the sensitivity to uncertainties in the source redshift distribution. Combined with advances in shape measurements we estimate that the systematic uncertainties in the lensing signal are less than 3%, sufficient for the size of the MENeaCS sample. We compute physical cluster properties by fitting parametric models to the contamination corrected weak lensing signal. The weak lensing masses and velocity dispersions are in fair agreement with estimates based on galaxy dynamics and we find consistent relations for MENeaCS and the Canadian Cluster Comparison Project. We derive a scaling relation with hydrostatic masses using *Planck* measurements and find a bias in the hydrostatic masses $1 - b = 0.90 \pm 0.05(\mathrm{stat}) \pm 0.03(\mathrm{syst})$ when combining both cluster samples. The data support a decreasing trend of $1 - b$ with mass, which is in agreement with other observations.

R. Herbonnet, C. Sifón, H. Hoekstra, R. F. J. Van der Burg
to be submitted

4.1 Introduction

The growth rate of massive structures is sensitive to cosmology as gravitational build-up of overdensities in the initial density distribution is counteracted by the expansion of the Universe. Numerical simulations can predict the abundance of massive structures for varying cosmologies and linking these to such objects in the real Universe allows for cosmological tests. Although the bulk of the mass in these structures is in the form of dark matter, they are observable across the electro-magnetic spectrum because they contain large amounts of baryons that manifest their presence in various ways, such as clusters of galaxies and hot gas. Studies of the number of clusters as a function of mass and redshift (cluster mass function) have put tight constraints on the energy density of matter Ω_m and normalisation of the matter power spectrum σ_8 and the redshift evolution of the mass function can constrain the abundance and the equation of state of dark energy and the number of neutrino species (Borgani & Guzzo 2001; Vikhlinin et al. 2009b; Planck Collaboration et al. 2014; Mantz et al. 2015; Planck Collaboration et al. 2016b; de Haan et al. 2016). See also Allen et al. (2011) for a general review on galaxy clusters as a cosmological tool.

Determination of the cluster mass function requires a large sample of clusters representative of the whole population *and* accurate mass estimates of those clusters. The number of observed clusters is steadily increasing thanks to optical searches for overdensities of (red) galaxies (e.g. Gladders & Yee 2005; Rykoff et al. 2016), and X-ray surveys looking for diffuse hot intracluster gas (e.g. Böhringer et al. 2004; Vikhlinin et al. 2009a). In recent years millimeter wavelength observations have added greatly to the number of detected clusters (Hasselfield et al. 2013; Bleem et al. 2015; Planck Collaboration et al. 2016c). In galaxy clusters photons from the cosmic microwave background (CMB) undergo inverse Compton scattering off the hot intracluster gas thereby obtaining a slight net boost in energy (Sunyaev & Zeldovich 1972, SZ). This SZ effect introduces a characteristic distortion in the millimetre part of the spectral energy distribution, which is a tell-tale sign of a massive galaxy cluster. CMB photons are present at all observable redshifts and the SZ signal scales linearly with gas density making it observable even for high redshift clusters with relatively low gas density.

All these surveys detect clusters based on a selection function (such as signal to noise ratio cuts), which can make the sample unrepresentative of the underlying distribution of clusters. The selection function needs to be taken into account, lest the cluster mass function be biased (see e.g. Mantz et al. 2010; Battaglia et al. 2016 for the effects of selection functions).

The second requirement for robust estimates of cosmological parameters is a well calibrated relation between survey observable and mass[1]. In fact, the lack of a reliable scaling relation is the main limitation for the full exploitation of the all-sky *Planck* cluster catalogue. The total mass of clusters can be computed using kinematics of cluster members under the assumption of dynamical equilibrium (e.g. Ruel et al. 2014; Bocquet et al. 2015; Sifón et al. 2016; Amodeo et al. 2017) or using caustics (Rines et al. 2016). The X-ray temperature and surface brightness profile can be connected to mass, but this is usually done under the assumption of hydrostatic equilibrium (see e.g. Battaglia et al. (2012) for an assessment of the impact of non thermal pressure on cluster mass estimation). As clusters formed through mergers, most clusters will not be in a state of equilibrium. Numerical hydrodynamical simulations consistently suggest

[1] Actually, because of degeneracy between cosmological and astrophyical parameters in the estimation, the scaling relation should be inferred simultaneously with cosmological parameters (Mantz et al. 2010, e.g.)

that X-ray masses can be biased low by ~10%-35% depending on the dynamical state of the cluster (Nagai et al. 2007; Rasia et al. 2012; Henson et al. 2017).

Weak gravitational lensing can provide the total mass of a cluster against which other mass proxies can be calibrated. A galaxy cluster acts as a lens because its gravitational potential distorts the surrounding space-time which deflects photons from their straight line trajectories. This phenomenon introduces a coherent distortion (shear) in the observed shape of background galaxies. The lensing signal is not sensitive to the dynamical state of the cluster and can be a source for unbiased mass estimates. However, lensing is a probe for the gravitational potential projected along the line of sight and the triaxial distribution of mass introduces an uncertainty of ~10-30% in the weak lensing estimates (Corless & King 2007; Meneghetti et al. 2010; Becker & Kravtsov 2011; Rasia et al. 2012; Henson et al. 2017). Moreover, uncorrelated large scale structure also affects the lensing signal introducing extra scatter in the mass estimates (Hoekstra 2001; Hoekstra et al. 2011a). For a large sample of clusters these uncertainties should average out, so reliable scaling relations can only be produced for large samples of clusters.

A number of studies have estimated weak lensing masses for galaxy clusters with the aim to constrain scaling relations (Jee et al. 2011; Okabe et al. 2013; von der Linden et al. 2014b; Kettula et al. 2015; Hoekstra et al. 2015; Okabe & Smith 2016; Penna-Lima et al. 2016; Schrabback et al. 2016; Sereno et al. 2017). The large numbers of studied clusters help to reduce the statistical uncertainties, but also to quantify the intrinsic scatter of the scaling relations, which can help to reveal the underlying astrophysical origins. The largest weak lensing surveys have targeted several tens of galaxy clusters so that statistical errors can become comparable to systematic uncertainties. Therefore, the main focus for the Weighing the Giants survey (WtG, von der Linden et al. 2014a; Applegate et al. 2014), the Canadian Cluster Comparison Project (CCCP, Hoekstra et al. 2012, 2015), the Local Cluster Substructure Survey (LoCuSS, Okabe & Smith 2016) and Cluster Lensing and Supernovae survey with Hubble (CLASH, Umetsu et al. 2014) has been to robustly assess sources of systematic errors. Weak lensing experiments measure the shear by averaging the shapes of galaxies behind the clusters, and combine these with distance estimates for the background galaxies in order to reconstruct the mass profile. The background galaxies are predominantly faint objects, so the distances are computed using photometric redshifts. Systematics are thus introduced by biased measurements of the galaxy shapes or of the galaxy redshifts, a false classification of objects as background galaxies, and an incorrect estimation of the mass profile. These effects have become more important as different teams have found inconsistent mass estimates for the same clusters. To investigate the discrepancies between Applegate et al. (2014) and Hoekstra et al. (2012), the CCCP cluster mass estimates were revisited by Hoekstra et al. (2015, hereafter H15). They used a large set of simulations of telescope images to calibrate their shape measurement algorithm to an accuracy of 2%. Unlike the WtG data, the CCCP data did not have enough colour data for their galaxies to compute photometric redshifts. This lack of redshifts was a major concern, but was overcome with a separate high fidelity redshift catalogue and a correction for the contaminated sample of background galaxies. With these improvements they found that shear- and masses estimates were consistent between the two teams within the measurement uncertainties.

With the robust pipeline of H15, systematic errors are low enough that they are comparable to the statistical uncertainties. In this work, we build on the work of H15 by studying another sample of clusters, which was observed with the Canada-France-

Hawaii Telescope (CFHT), as was CCCP, and analyse it with the same pipeline. The Multi Epoch Nearby Cluster Survey (MENeaCS) provides excellent quality optical imaging data in the g and r-band for a sample of 58 X-ray selected clusters at $0.05 < z < 0.15$. MENeaCS presents a significant collection of clusters allowing for a precise determination of the average cluster mass. However, as was the case for CCCP, the trade-off for the large sample size is the lack of colour information required to estimate photometric redshifts for all observed galaxies. Fortunately, the systematic errors due to the lack of individual redshifts are much less severe thanks to the low redshifts of the clusters compared to the CCCP analysis. The local MENeaCS cluster galaxies are spread over a larger part of the sky and thus the number density of cluster members contaminating the background population should be small. The lensing signal for low redshift clusters is also fairly insensitive to the actual distribution of redshifts of background galaxies (Hoekstra et al. 2011a). These qualities make MENeaCS an excellent sample of galaxy clusters with which to estimate robust weak lensing masses.

The MENeaCS observations are briefly described in Section 4.2, where we also present details on the pipeline used to determine galaxy shapes. The MENeaCS observations lack the colour information required for accurate photometric redshifts and instead we determine a distribution of redshifts for the background galaxy population using ancillary data. This process is described in Section 4.3. Without reliable photometric redshifts, galaxies cannot be separated into a population associated to the cluster and a population of gravitationally lensed background galaxies. We derive a correction for this contamination in Section 4.4. In Section 4.5 we determine the physical properties of the MENeaCS clusters by fitting parametric density models to the corrected weak lensing signal. We then assess the robustness of our results by comparing them against estimates derived using galaxy dynamics. Finally we compute a scaling relation with the masses estimated using the *Planck* CMB measurements (Planck Collaboration et al. 2016c) and we conclude in Section 4.6. Throughout the paper we assume a flat Λ cold dark matter cosmology where $H_0{=}70h_{70}$ km/s/Mpc and the current energy densities of matter and dark energy are $\Omega_m(z = 0) = 0.3$ and $\Omega_\Lambda(z = 0) = 0.7$, respectively. All masses and radii scale as h_{70}^{-1}.

4.2 Data and shape analysis

The Multi Epoch Nearby Cluster Survey (MENeaCS) is a deep, wide-field imaging survey of a sample of X-ray selected clusters with $0.05 < z < 0.15$. The data were obtained with two main science objectives in mind. The first, the study of the dark matter halos of cluster galaxies using weak gravitational lensing, defined the required total integration time and image quality, as well as the redshift range; with ground-based observations such studies are best done with low redshift clusters. The results of this analysis are presented in **Chapter 5**. Taking advantage of the queue scheduling of CFHT observations, however, the observations were spread over a two-year period, which enabled a unique survey to study the rate of supernovae in clusters (Sand et al. 2012; Graham et al. 2012), including intra-cluster supernovae (Sand et al. 2011). To do so, typically two 120s exposures in the g and r-band were obtained for each epoch (which are a lunation apart). The full sample comprises the 58 most X-ray luminous clusters that were catalogued at the start of the survey, whilst observable with the CFHT. A detailed description of the survey is presented in Sand et al. (2012)[2]. All

[2]We note that Sand et al. (2012) did not present results for Abell 401, which we have included in the total sample.

clusters used in our analysis are listed in Table 4.1 together with their redshift and the coordinates of the brightest cluster galaxy (BCG) which we take as the centre of the cluster. A possible complication is the misclassification of a galaxy as the BCG (see e.g. Bildfell et al. 2008). However, it was straightforward for the MENeaCS clusters from visual inspection which galaxy was the BCG.

In this paper we use the r-band data to determine the cluster masses using weak gravitational lensing. The individual exposures are pre-processed using the `Elixir` pipeline (Magnier & Cuillandre 2004), and we refine the astrometry using `Scamp` (Bertin 2006). Although the CFHT observations were typically obtained when the seeing was below $1''$, some exposures suffer from a larger PSF. As this is detrimental for accurate shape measurements, these exposure were excluded when co-adding the data. For each cluster the 20 frames with the best image quality were selected and combined into a single deep mosaic using `Swarp` (Bertin 2010). However, if additional frames had a seeing full width at half maximum less than 0.80 arcseconds they were added to the stack. The minimal depth of each mosaic is 40 minutes of exposure time. The magnitudes we use are corrected for Galactic extinction using the Schlafly & Finkbeiner (2011) recalibration of the Schlegel et al. (1998) infrared-based dust map. For the analysis presented here, we excluded 9 clusters based on their r-band Galactic dust extinction A_r. The threshold value $A_r < 0.2$ was chosen to reflect the range in which we can reliably correct for contamination (see Section 4.4 and Appendix 4.A). Finally, the cluster Abell 763 contained no significant overdensity of galaxies and was removed from the sample. Table 4.1 lists for all selected clusters the characteristics of the image quality of the mosaic: the half-light radius of the PSF, the root mean square (r.m.s.) noise level and the Galactic extinction.

Objects were detected in the mosaics using the pipeline described in Hoekstra et al. (2012). To measure the weak lensing signal around the clusters we select objects with an r-band magnitude $20 \leq m_r \leq 24.5$. Following H15 an upper limit of 5 pixels on the galaxy half-light radius is imposed. A lower limit for the size is set by the size of the PSF, which removes stars and small galaxies that have highly biased shapes. Galaxies are assigned a lensing weight

$$w = \left[\langle \epsilon_{\rm int}^2 \rangle + \left(\frac{\sigma_\chi}{P^\gamma} \right)^2 \right]^{-1}, \tag{4.1}$$

where $\langle \epsilon_{\rm int}^2 \rangle = 0.25^2$ is the dispersion in the distribution of intrinsic ellipticities and σ_χ is an estimate of the uncertainty in the measured polarisation value χ due to noise in the image (Hoekstra et al. 2000). The polarisation is measured using a weight function to reduce the effect of noise, which introduces a bias in the final shear estimate. The shear polarisability P^γ corrects the polarisation for the use of the weight function and for PSF smearing. The shear is then computed as the weighted average of the corrected polarisations

$$g_i = \frac{\sum\limits_n w_n \chi_{i,n} / P_n^\gamma}{\sum\limits_n w_n}, \tag{4.2}$$

where the index i indicates the two Cartesian components of the shear and the sum runs over all galaxies in the sample. In practice, we measure the reduced shear $g_i = \gamma_i/(1-\kappa_i)$ (Bartelmann & Schneider 2001), which deviates from the true shear γ near the cluster centre, but for most radii of interest the convergence κ is negligible, although we take it into account in our analysis. We decompose the shear into a cross and tangential component relative to the lens, where the tangential shear $g_{\rm t}$ can be related to the

projected mass of the lens and the cross shear can be used to find systematic errors (Schneider 2003).

The galaxy polarisations and polarisabilities are measured from the mosaics using the shape measurement algorithm detailed in H15, which is based on the moment-based method of Kaiser et al. (1995). H15 used extensive image simulations to quantify the multiplicative bias that arises from noise in the data and the imperfect correction for the blurring by the PSF. The MENeaCS data are similar in terms of depth and image quality compared to the observations of the CCCP that were analysed in H15; therefore we use the same correction scheme. A potentially important difference with the CCCP analysis is that the individual exposures are offset from one another. This could lead to a complicated PSF pattern in the combined images. However, tests on the CCCP data indicate that this results in a negligible change in the mass estimates. Moreover, the large number of exposures, combined with the smooth PSF pattern results in a smooth PSF when measured from the mosaics.

Galaxy magnitudes are corrected for background light by subdividing pixels without galaxy light in an annulus between 16 and 32 pixels into four quadrants and fitting the quadrants with a plane to allow for spatial variation of the background. We found that bright neighbouring objects affect this local background subtraction, which in turn affects the shape measurement. When we examined the performance of the algorithm near bright cluster members in image simulations for the purpose of studying the lensing signal around such galaxies (see **Chapter 5**), there were cases where $m_{\rm find}$, the apparent magnitude as measured by the detection algorithm differed from $m_{\rm shape}$, the magnitude measured by the shape measurement algorithm. No background light was present in the simulations and instead the local background subtraction was affected by the proximity of bright cluster galaxies. We introduced a flag that identified galaxies for which the shape measurement is biased due to the background subtraction. A cut based on $\Delta m = m_{\rm find} - m_{\rm shape}$ of

$$\Delta m > -49.0 - 7.0\, m_{\rm shape} + 0.3\, m_{\rm shape}^2 - 0.005\, m_{\rm shape}^3 \tag{4.3}$$

efficiently removed problematic objects. We therefore apply this cut to the full lensing catalog, which removes approximately 10% of the sources. We applied the same selection to the image simulations studied in H15 and found that the biases are unchanged. Consequently, we use the same parameters to correct for the biases in the method. H15 estimate that the systematic uncertainties in the cluster masses caused by the shape measurements is less than 2%, which is also adequate for the results presented here.

4.3 Photometric source redshift distribution

Gravitational lensing is a geometric phenomenon and the amplitude of the effect depends on the distances involved. This dependency is parametrised by the critical surface density

$$\Sigma_{\rm crit} = \frac{c^2}{4\pi G} \frac{D_{\rm os}}{D_{\rm ol}\, D_{\rm ls}}, \tag{4.4}$$

where the lensing efficiency $\beta = \max(0, D_{\rm ls}/D_{\rm os})$ contains the redshift information about the background galaxy (termed the 'source'). The angular diameter distances $D_{\rm os}, D_{\rm ls}, D_{\rm ol}$ are measured between observer 'o', lens 'l' and/or source 's'. The definition of β is such that objects in front of the cluster, which are not gravitationally sheared,

do not contribute to the measured signal. For an increasing source redshift the lensing efficiency β rises sharply when the source redshift is comparable to the lens redshift, but it flattens off when source and lens are far apart.

We lack photometric redshifts for individual objects in our catalogue and we cannot determine the critical surface density for each source lens pair. However, as the galaxies are averaged to obtain a shear estimate, we can use the average lensing efficiency $\langle\beta\rangle$ to compute the critical surface density for the full source population. This assumption introduces a bias in our shear estimates which can be approximately corrected for by multiplying our reduced shear estimates by

$$1 + \left(\frac{\langle\beta^2\rangle}{\langle\beta\rangle^2} - 1\right)\kappa, \tag{4.5}$$

(Equation 7 in Hoekstra et al. 2000). The width of the distribution of the lensing efficiency $\langle\beta^2\rangle$ corrects the reduced shear for the use of a single value of $\langle\beta\rangle$. For our local clusters most sources are so distant that there is little variation in the value of β. Indeed, we find that the ratio $\langle\beta^2\rangle/\langle\beta\rangle^2 \approx 1$ in the range $0.05 \leq z \leq 0.15$ and so the correction is negligible for our analysis. However, when we compute cluster properties we do correct our reduced shear estimates using Equation 4.5 for completeness.

A reference sample of field galaxies can serve as a proxy for the source population in the observations from which the average lensing efficiency can be computed. For this we use the Cosmological Evolution Survey (COSMOS) field which has received dedicated spectroscopic coverage so that reliable redshift estimates are available. In our analysis we use the COSMOS2015 catalogue of Laigle et al. (2016), which contains photometric redshifts of galaxies in the COSMOS field based on over 30 different wavelengths. This catalogue has two important benefits for our analysis. First, near infrared data from the UltraVISTA DR2 are included, so that the Lyman and Balmer/4000 Å breaks can be distinguished. The additional knowledge on these features helps to robustly assess high redshift galaxies, which would otherwise tend to be assigned a low redshift. Second, the catalogue also includes the CFHT r filter, so that we can easily match it to our data. Although the objects in the COSMOS2015 catalogue were not selected based on their r-band magnitude, we find that the catalogue is complete down to $m_r \approx 25$, which is sufficient to cover our magnitude range $20 \leq m_r \leq 24.5$. From comparisons to spectroscopic data Laigle et al. (2016) found that their redshift estimates are accurate to better than a percent, which is sufficient for this study.

However, the COSMOS2015 catalogue is not representative of our MENeaCS lensing catalogues, as the latter are subject to various cuts. Gruen & Brimioulle (2016) have shown that these selection effects can introduce a bias in the mass estimates. To quantify the impact, we ran our lensing pipeline on r-band observations of the CFHT Legacy Survey (CFHTLS) D2 field which covers ~1 square degree of the COSMOS field and matched the lensing catalogue to the COSMOS2015 catalogue. This enabled us to perform exactly the same cuts on the redshift distribution as were applied to the lensing data. We found that applying the cuts introduces a difference in the lensing efficiency of only $\Delta\beta \leq 1\%$ for all clusters. We use the matched catalogue for our analysis, but note that this does not significantly impact our results, nor the results in H15.

We select galaxies from the matched catalogue using the `TYPE` parameter, which classifies objects as either stars or galaxies. The observed galaxy density as function of magnitude varies for the MENeaCS clusters due to the different observing conditions,

which is not reflected in the source population in COSMOS. As a galaxy's magnitude depends on its redshift, using the COSMOS galaxies to compute $\langle\beta\rangle$ directly may lead to an incorrect value for our data. Therefore we customise our COSMOS galaxy population by reweighting them to match the magnitude distributions for individual MENeaCS clusters. The redshift catalogue is divided into magnitude bins and for each magnitude bin we compute the sum of the lensing weights of the COSMOS galaxies (as the appropriate proxy for number of galaxies) and the mean lensing efficiency $\langle\beta\rangle_{\rm bin}$. Then the final estimate $\langle\beta\rangle$ for each cluster is the average of $\langle\beta\rangle_{\rm bin}$ weighted by the sum of the lensing weight for all bins. For each cluster the value of $\langle\beta\rangle$ is listed in column 9 of Table 4.1. We use $\langle\beta\rangle$ to compute the average critical surface density with which we estimate cluster masses. In order to apply Equation 4.5 we also require $\langle\beta^2\rangle$, which is calculated the same way and listed in column 10 of Table 4.1.

The redshift distribution in our catalogue based on 1 square degree of the COSMOS field might not be representative for all source populations in our observations. This cosmic variance introduces an uncertainty in the mean lensing efficiency $\langle\beta\rangle$. We estimate the impact of cosmic variance using the photometric redshift catalogues of Coupon et al. (2009) for the four CFHTLS DEEP fields. We also analysed these fields with our own weak lensing pipeline and matched these catalogues to introduce the lensing selections. These photometric redshifts are based on five optical bands and hence are not as reliable as the COSMOS2015 catalogue. However, as the four fields were analysed consistently they may serve as an estimate of the variation in redshift distributions due to cosmic variance. For each cluster we compute the weighted average $\langle\beta\rangle$ for the 4 fields and use the standard deviation between them as the error due to cosmic variance.

In addition to cosmic variance, there are Poisson errors in the $\langle\beta\rangle$ due to finite statistics. The Poisson errors are estimated by comparing the lensing efficiency in the CFHTLS D2 field with the lensing efficiency in the remainder of the COSMOS field, where we assume that within two square degrees cosmic variance is subdominant. We compare the lensing efficiency for galaxies between $20 \leq m_r \leq 24.5$ for both regions and use the difference as a measure of the Poisson error. As we do not have KSB parameters for the full COSMOS2015 catalogue we do not impose any other constraints besides the magnitude limits. We assume that the lensing cuts would affect both samples in the same way.

The uncertainties from cosmic variance and finite statistics are roughly equal in amplitude and we estimate our final uncertainty by summing both quadratically, assuming they are independent. The uncertainty in the average lensing efficiency for each cluster is listed in column 6 in Table 4.1 and is at most ~1.5%. Strictly speaking, this is a conservative estimate, as our cosmic variance errors are also affected by Poisson errors. An error $\delta\beta \sim 1.5\%$ is a marked improvement over H15 who found an uncertainty of 4.2%. In part, this can attributed to our use of better photometric redshift data. However, H15 found that most of their uncertainty was driven by faint galaxies and the shallower data for MENeaCS help to reduce the error. Finally, for the low redshift MENeaCS clusters the distribution of β is very peaked which reduces the uncertainty in the lensing efficiency.

(1)	(2) cluster	(3) z	(4) $\mathrm{RA}^{\mathrm{BCG}}$ (J2000)	(5) $\mathrm{Dec}^{\mathrm{BCG}}$ (J2000)	(6) A_r [mag]	(7) R_{PSF} [pixels]	(8) r.m.s. noise [counts]
1	A7	0.106	00:11:45.2	+32:24:56.4	0.086	1.907	1.279
2	A21	0.095	00:20:37.3	+28:39:28.3	0.083	2.005	1.325
3	A85	0.055	00:41:50.4	−09:18:11.3	0.082	1.964	1.447
4	A119	0.044	00:56:16.1	−01:15:19.1	0.084	2.041	1.403
5	A133	0.057	01:02:41.7	−21:52:54.4	0.040	2.148	1.405
6	A646	0.129	08:22:09.5	+47:05:52.9	0.089	2.171	1.381
7	A655	0.127	08:25:29.0	+47:08:00.4	0.076	2.056	1.389
8	A754	0.054	09:08:32.3	−09:37:47.4	0.150	2.338	1.326
9	A780	0.054	09:18:05.7	−12:05:45.2	0.086	2.542	1.470
10	A795	0.136	09:24:05.3	+14:10:21.8	0.062	2.282	1.514
11	A961	0.124	10:16:22.8	+33:38:17.3	0.039	2.245	1.536
12	A990	0.144	10:23:39.8	+49:08:37.8	0.014	2.468	1.482
13	A1033	0.126	10:31:44.2	+35:02:28.0	0.037	2.064	1.627
14	A1068	0.138	10:40:44.5	+39:57:11.2	0.046	1.937	1.582
15	A1132	0.136	10:58:23.6	+56:47:41.8	0.024	2.144	1.600
16	A1285	0.106	11:30:23.8	−14:34:52.8	0.090	2.587	1.588
17	A1348	0.119	11:41:24.2	−12:16:38.5	0.066	2.590	1.535
18	A1361	0.117	11:43:39.5	+46:21:20.4	0.050	1.926	1.401
19	A1413	0.143	11:55:18.0	+23:24:18.6	0.052	2.074	1.423
20	A1650	0.084	12:58:41.5	−01:45:40.9	0.036	2.413	1.316
21	A1651	0.085	12:59:22.4	−04:11:45.8	0.060	2.871	1.625
22	A1781	0.062	13:44:52.5	+29:46:15.3	0.035	2.308	1.199
23	A1795	0.062	13:48:52.5	+26:35:33.2	0.028	2.162	1.402
24	A1927	0.095	14:31:06.7	+25:38:01.3	0.084	1.953	1.284
25	A1991	0.059	14:54:31.4	+18:38:32.3	0.071	2.116	1.465
26	A2029	0.077	15:10:56.1	+05:44:41.0	0.083	2.058	1.330
27	A2033	0.082	15:11:26.5	+06:20:56.7	0.081	1.937	1.237
28	A2050	0.118	15:16:17.9	+00:05:20.8	0.119	1.953	1.296
29	A2055	0.102	15:18:45.7	+06:13:56.2	0.082	1.935	1.300
30	A2064	0.108	15:20:52.2	+48:39:38.4	0.036	2.196	1.129
31	A2065	0.073	15:22:29.1	+27:42:27.6	0.086	2.079	1.230
32	A2069	0.116	15:24:07.4	+29:53:20.2	0.053	1.945	1.152
33	A2142	0.091	15:58:20.0	+27:14:00.3	0.098	1.971	1.259
34	A2420	0.085	22:10:18.7	−12:10:13.7	0.127	2.130	1.638
35	A2426	0.098	22:14:31.5	−10:22:26.2	0.129	2.293	1.757
36	A2440	0.091	22:23:56.9	−01:34:59.7	0.174	2.200	1.449
37	A2443	0.108	22:26:07.8	+17:21:23.4	0.136	1.944	1.352
38	A2495	0.078	22:50:19.7	+10:54:14.1	0.167	1.938	1.366
39	A2597	0.085	23:25:19.7	−12:07:27.0	0.066	2.106	1.649
40	A2627	0.126	23:36:42.0	+23:55:29.0	0.168	2.025	1.360
41	A2670	0.076	23:54:13.6	−10:25:08.5	0.097	2.422	1.520
42	A2703	0.114	00:05:23.9	+16:13:09.2	0.103	1.881	1.326
43	MKW3S	0.045	15:21:51.8	+07:42:31.8	0.077	2.046	1.253
44	RXJ0132	0.149	01:32:41.1	−08:04:04.8	0.066	1.901	1.444
45	RXJ0736	0.118	07:36:38.0	+39:24:52.6	0.104	2.198	1.418
46	RXJ2344	0.079	23:44:18.2	−04:22:49.1	0.077	2.198	1.515
47	ZWCL1023	0.143	10:25:57.9	+12:41:08.4	0.101	2.274	1.528
48	ZWCL1215	0.075	12:17:41.1	+03:39:21.2	0.036	2.730	1.484

(1)	(2) cluster	(3) z	(9) $\langle\beta\rangle$	(10) $\langle\beta^2\rangle$	(11) $\delta\beta$
1	A7	0.106	0.714	0.536	0.008
2	A21	0.095	0.738	0.568	0.007
3	A85	0.055	0.841	0.718	0.004
4	A119	0.044	0.871	0.767	0.004
5	A133	0.057	0.834	0.708	0.005
6	A646	0.129	0.665	0.469	0.009
7	A655	0.127	0.669	0.475	0.008
8	A754	0.054	0.842	0.720	0.005
9	A780	0.054	0.841	0.718	0.005
10	A795	0.136	0.648	0.449	0.010
11	A961	0.124	0.675	0.481	0.008
12	A990	0.144	0.632	0.428	0.010
13	A1033	0.126	0.670	0.475	0.008
14	A1068	0.138	0.646	0.446	0.010
15	A1132	0.136	0.648	0.448	0.010
16	A1285	0.106	0.709	0.528	0.009
17	A1348	0.119	0.683	0.492	0.007
18	A1361	0.117	0.693	0.505	0.007
19	A1413	0.143	0.636	0.434	0.010
20	A1650	0.084	0.763	0.603	0.007
21	A1651	0.085	0.756	0.592	0.007
22	A1781	0.062	0.821	0.688	0.005
23	A1795	0.062	0.821	0.688	0.005
24	A1927	0.095	0.740	0.571	0.007
25	A1991	0.059	0.828	0.698	0.005
26	A2029	0.077	0.782	0.631	0.007
27	A2033	0.082	0.772	0.615	0.006
28	A2050	0.118	0.690	0.502	0.008
29	A2055	0.102	0.724	0.548	0.008
30	A2064	0.108	0.710	0.530	0.008
31	A2065	0.073	0.793	0.646	0.007
32	A2069	0.116	0.696	0.510	0.007
33	A2142	0.091	0.747	0.581	0.007
34	A2420	0.085	0.759	0.597	0.007
35	A2426	0.098	0.726	0.551	0.007
36	A2440	0.091	0.745	0.577	0.007
37	A2443	0.108	0.708	0.527	0.008
38	A2495	0.078	0.778	0.625	0.007
39	A2597	0.085	0.760	0.598	0.007
40	A2627	0.126	0.672	0.478	0.008
41	A2670	0.076	0.780	0.628	0.007
42	A2703	0.114	0.699	0.513	0.007
43	MKW3S	0.045	0.868	0.763	0.004
44	RXJ0132	0.149	0.622	0.419	0.010
45	RXJ0736	0.118	0.686	0.497	0.008
46	RXJ2344	0.079	0.775	0.620	0.007
47	ZWCL1023	0.143	0.633	0.430	0.010
48	ZWCL1215	0.075	0.783	0.631	0.007

Table 4.1: Basic information on the MENeaCS clusters, parameters governing the quality of our observations and the lensing efficiency β computed in Section 4.3. (2 & 3) cluster name and redshift; (4)&(5) coordinates of the BCG, which is taken to be the cluster centre; (6) Galactic extinction in r-band magnitude; (7) half-light radius of the PSF in pixels averaged over the entire image; (8) r.m.s. of the background noise in counts; (9) average β used to estimate the critical surface density; (10) average β^2 used to correct the shear for the lack of individual source redshifts; (11) error on β (see text for more details).

4.4 Contamination of the source population by cluster members

The galaxy catalogue from the lensing analysis contains both field galaxies and cluster members. Cluster members are not sheared by the gravitational potential of the cluster and keeping them in the sample will alter the shear signal. If cluster galaxies are not intrinsically aligned (as has been shown by Sifón et al. 2015), their presence dilutes the shear signal, biasing the shear estimate low, where the size of the bias depends on the relative overdensity of cluster members compared to background galaxies. At low redshift, cluster galaxies are spread out over the field of view, so their number density per unit solid angle is low.

With reliable redshifts for individual galaxies, cluster members can be identified and removed from the sample. However, we lack the multi-band observations to acquire reliable photometric estimates. Instead, we can apply a 'boost correction' to statistically correct for cluster member contamination (see appendix A1 of Leauthaud et al. (2016) for a discussion of the boost correction). This approach offsets the dilution of the shear by boosting the shear signal based on the fraction of cluster members to background galaxies. The application of the boost correction relies on the assumption that only cluster members affect the galaxy counts. We investigate the effects that violate this assumption in the next sections and take them into account to obtain a reliable estimate of the density of cluster members relative to the density of background galaxies, from which we compute the boost correction.

As noted in Section 4.2 close proximity to bright objects can affect the measured shapes of galaxies, changing the measured shear signal. We incorporate this effect by quantifying the boost correction in terms of the sum of the lensing weights per square arcminute, which we call the weight density ξ.

4.4.1 Magnification

Gravitational lensing near the cluster core magnifies the background sky. This phenomenon increases the observed flux of background galaxies, but it also reduces the actual area behind the cluster that is observed. These two features counteract each other in their effect on the observed number density of sources. The net effect depends on the number of galaxies scattered into the magnitude range that we designate for our lensing study. The observed number of galaxies increases with the magnification μ as $\mu^{2.5\alpha-1}$ (Mellier 1999). Hence, for a slope of the magnitude distribution $\alpha = \mathrm{d}\log N_{\mathrm{source}}/\mathrm{d}m_{\mathrm{shape}} = 0.40$ the net effect is negligible. For the MegaCam r-band data H15 computed that the slope is close to 0.40 and so we can safely ignore the effect of magnification on the source population.

4.4.2 Obscuration

Cluster members are large foreground objects and obscure part of the background sky, thereby reducing the number density of observed background galaxies. This phenomenon is especially important for MENeaCS as the low redshift cluster members are very spread out. As the cluster member density increases towards the cluster core, obscuration reduces the apparent contamination signal as a function of projected cluster-centric distance. To address this issue we use the results of **Chapter 5**, where we used image simulations of the MENeaCS clusters to compute the effect of obscuration. Their cluster image simulations were designed to mimic the observations as

closely as possible to accurately predict the effect of obscuration. For each simulated cluster image the seeing and noise level were set to the values measured in the data. Background galaxies were created with the image simulations pipeline of H15, which is based on the GalSim software (Rowe et al. 2015), and cluster galaxies were added to the images. Where available, the GALFIT (Peng et al. 2002) measurements of Sifón et al. (2015) were used to create surface brightness profiles for cluster members, which were identified through spectroscopy or as part of the red sequence. For cluster members without (reliable) GALFIT measurements, galaxy properties were randomly sampled from parametric curves which follow the observed distributions of those properties. The analysis pipeline is run on both the background image and the cluster image producing two lensing catalogues. By matching these catalogues all background galaxies can be selected and the effect of cluster members on the weight density of the background population can be determined. The obscuration is defined as

$$f_{\rm obsc} = 1 - \frac{\xi^{\rm cl}}{\xi^{\rm bg}}, \tag{4.6}$$

where $\xi^{\rm cl}$ and $\xi^{\rm bg}$ are the weight densities of all observed background galaxies in the cluster simulation and in the background simulation, respectively.

In Figure 4.1 we show the resulting obscuration in bins of projected cluster centric distance for individual clusters R in gray, and in black the average for all clusters. The effect of obscuration is greatest in the very lowest radial bins, which is expected because of the presence of the low redshift BCGs. At radii larger than 1 Mpc the obscuration flattens out but does not reach zero. We do not expect cluster members to obscure ∼5% of all background galaxies in these outer regions. Instead, this plateau is caused by field galaxies entering the cluster member sample, as Sifón et al. (2015) showed that their sample of red sequence selected cluster members is contaminated at large radii. The simulated sample of cluster members lacks faint blue galaxies, but we expect that their obscuration is minimal and we thus ignore their contribution.

We determine an obscuration correction for the background weight density in the MENeaCS data by fitting a smooth function to the individual cluster obscuration profiles shown in gray in Figure 4.1. We find that the expression

$$f_{\rm obsc}(R) = n_\Delta + n_0 \left(\frac{1}{R + R_{\rm c}} - \frac{1}{R_{\rm max} + R_{\rm c}} \right), \tag{4.7}$$

worked well to describe the obscuration. We use the same expression in Section 4.4.4 to model the contamination and we discuss it in more detail there. On average $R_{\rm c} \approx 0.04$ Mpc and $n_0 \approx 0.04$ for the best fits to the obscuration profiles. The parameter $R_{\rm max} = 3$ Mpc and n_Δ was fit but then set to zero to renormalise the data such that $f_{\rm obsc}$ is consistent with zero beyond 1.5 Mpc. The best fits to the obscuration profiles to individual clusters were then used to correct the background galaxy counts in the MENeaCS data.

4.4.3 Excess galaxy weight density

Now that we have a correction for the decreased weight density due to obscuration, we can determine the excess weight density of all sources in the MENeaCS lensing catalogues relative to the weight density of background objects as a function of cluster-centric distance. This then provides the boost correction for the shear signal to correct for contamination of the source sample by cluster members.

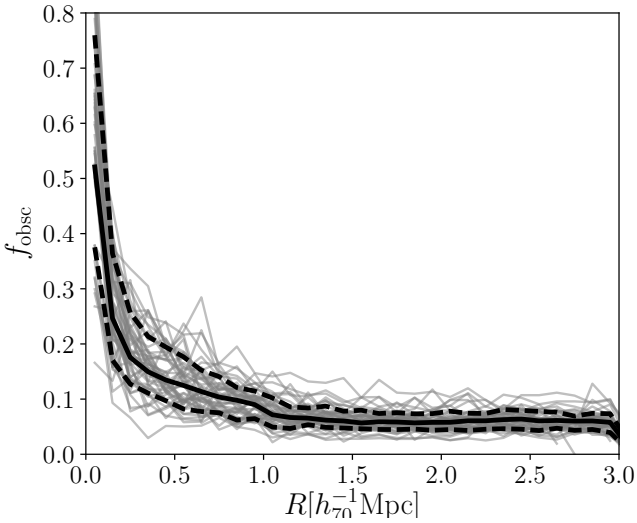

Figure 4.1: Fraction of source galaxies obscured by cluster members in realistic image simulations of MENeaCS clusters as a function of radial distance to the BCG, which is assumed to be the cluster centre. Gray lines show the obscuration profile for individual clusters and the black solid (dahsed) curve shows the average (1 σ spread) for all clusters. The region of interest for our lensing analysis is between 0.5 Mpc and 2 Mpc, where obscuration is on average a $\lesssim$10% effect.

The first step to compute the excess weight density is to determine the weight density of background objects. H15 computed that at 4 Mpc the structure associated to the cluster is a negligible contribution to the number density of field galaxies and used the area outside that 4 Mpc to estimate the galaxy density. The low redshift of the MENeaCS sample means that the field of view does not encompass 4 Mpc for all clusters. Only the clusters at $z > 0.1$ have any significant area outside 3 Mpc in the mosaics with full exposure time and only the highest redshift clusters have sufficient area outside 3 Mpc for statistically meaningful estimates. To compensate for this lack of data, we use ancillary publicly available observations of blank fields to obtain an estimate of the weight density of field galaxies (as was also suggested by Schrabback et al. 2016). We analysed ~33 square degrees of deep CFHT data with our lensing pipeline and we derive a parametric model for the field galaxy weight density $\xi^{\rm field}$ in Appendix 4.A. The value of $\xi^{\rm field}$ is a function of the Galactic extinction, depth of the observations, and the seeing, and it predicts the mean density with an uncertainty of 1%. We use this model to predict the weight density of field galaxies for each cluster based on the seeing, noise level and the Galactic extinction in the observations.

In Figure 4.2 we show the excess weight density $\xi/\xi^{\rm field}$ (the obscuration corrected weight density normalised to the weight density of field galaxies), as a function of the distance to the BCG. Points with errorbars show the average excess weight density for all clusters and blue (red) shaded regions show the average excess weight density for clusters at $z < 0.1$ ($z \geq 0.1$). The contamination by cluster members is benign for the MENeaCS clusters; the excess weight density is higher than 20% only within the inner 500 kpc. For the lensing analysis we only use sources beyond 500 kpc (see Section 4.5)

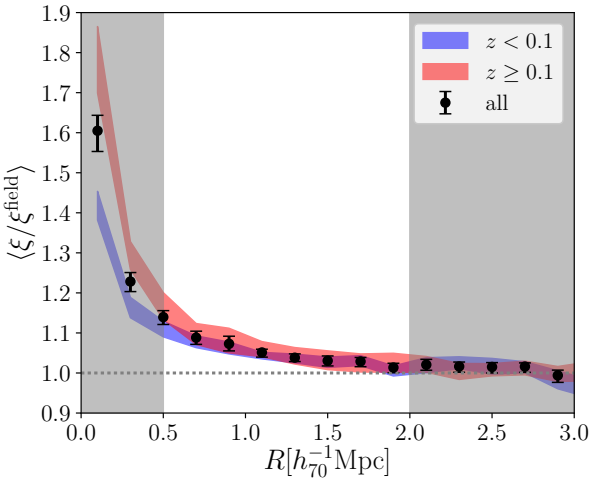

Figure 4.2: Excess weight densities of all sources in the magnitude range $20 \leq m_r \leq 24.5$ in the lensing catalogues as a function of radial distance to cluster centre, which we assume to be the position of the BCG. The excess weights are determined from the ratio of the weight density ξ corrected for obscuration and the average weight density for field galaxies. The blue (red) shaded area shows average excess weight density for all $z < 0.1$ ($z \geq 0.1$) clusters, black points with errorbars show the full MENeaCS sample. The dotted line shows unity. The width of the coloured regions and the errorbars show the 1 σ uncertainty in the excess weight density. The region shown in white between 0.5 Mpc and 2 Mpc is used for the lensing analysis, in which the contamination is on average ~5%.

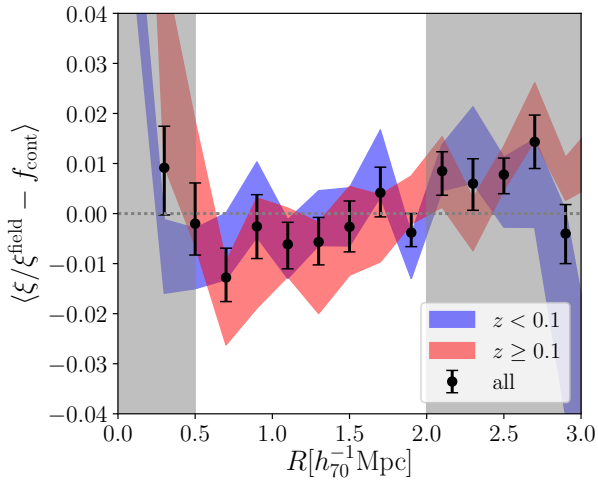

Figure 4.3: Average weight density of galaxies as a function of cluster-centric distance after the best fit model for contamination for each individual cluster has been subtracted. Blue (red) shaded area shows residual weight density for $z < 0.1$ ($z \geq 0.1$) clusters, points show the full MENeaCS sample. The width of the coloured regions and the errorbars show the 1 σ uncertainty. The region of interest for our lensing analysis is shown in white, where the residual contamination is consistent with zero.

and so the effect of contamination is small. The difference in the red and blue shaded regions clearly shows that this low level of contamination is thanks to the low redshift of the MENeaCS clusters.

The weight density from the blank fields predicts the average weight density of field galaxies very well, but it may not be representative of specific environments of the MENeaCS clusters. Specifically, we may miss large scale structure in the cluster background, which would have been properly accounted for if the density was normalised to the area outside the cluster. Therefore we checked the gain of combining the blank fields and any available area in the MENeaCS data outside 3 Mpc from the BCG for the highest redshift clusters. We redefined the field galaxy weight density $\xi^{\rm field}$ as the inverse variance weighted average of the blank fields and the available uncontaminated MENeaCS area. The spread of the blanks around the best fit is 6.4%, which is used as the square root of the variance for the blank fields. The variance for the uncontaminated data is estimated by subdividing the available area outside 3 Mpc into quadrants and taking the variance between the quadrants. The addition of the cluster data helps to reduce the uncertainty in the boost correction. However, in our analysis we are dominated by the uncertainty in the shear estimate due to the finite number of galaxies that are averaged. Hence we use the blank field prediction for $\xi^{\rm field}$ for all clusters to compute the excess weight density.

4.4.4 Boost correction

The excess weight density per cluster is a noisy measurement and using it directly to boost the shear signal can produce a spurious signal. Instead, we assume that the density of cluster members is a smooth function of the cluster-centric radius. This

assumption will not be valid if the cluster has local substructure, but any additional uncertainty this introduces, will average out for the full ensemble of clusters. A reasonable and simple approximation for the density of cluster members is the singular isothermal sphere (SIS; see also § 4.5.1). H15 found that the projected singular isothermal sphere was not able to describe the excess density profile to sufficient accuracy and introduced a function with additional parameters, which is shown in Equation 4.7. In this case, n_0 describes the amplitude of the contamination and the cluster core radius R_c is fitted for each cluster individually. The maximum radius R_{max} = 3 Mpc is the limit beyond which the function is set to n_Δ. In Figure 4.2 the excess weight density already vanishes beyond 2 Mpc, so setting R_{max} = 3 Mpc is reasonable for MENeaCS. All CCCP clusters were small enough in angular coordinates so that H15 could set n_Δ = 1. Our prediction for field galaxy weight density has an intrinsic scatter and so we do not expect the excess weight density for individual clusters to converge to 1 at large radii. Therefore we add n_Δ as a free parameter in our analysis. We find that the relative spread in n_Δ is 7.2%, which is in agreement with the 6.4% scatter expected from the blank fields.

The ensemble averaged residual, after subtracting the best fit profile for each cluster, is shown in Figure 4.3. Again, we separate the sample in low redshift ($z < 0.1$, blue) and high redshift ($z \geq 0.1$, red) clusters and the full sample is denoted by the black points. For most radii the average residual is consistent with zero within the errors, regardless of the mean redshift of the sample. This shows that Equation 4.6 is a decent description of the density of cluster members. At $R \approx 3$ Mpc the available area for $z < 0.1$ clusters is decreasing which greatly increases the errorbars and the crowded cluster centre is not accurately described by the fitting function. However, for the lensing analysis we restrict ourselves to 0.5 - 2 Mpc for which the residual is consistent with zero with an uncertainty of ~1%. The best fit profiles will serve as a boost correction for the shear signal of clusters to statistically correct for contamination of the source population by unlensed cluster members.

4.5 MENeaCS cluster masses

In the previous sections we have computed the corrections for the lack of individual redshift estimates for the source galaxies and the presence of cluster members in the source sample. We now apply these corrections to the measured tangential reduced shear and use the resulting shear as a function of cluster-centric distance to estimate the weak lensing masses.

To compute cluster masses we fit parametric models to our estimated shear profile. These symmetric models are not a perfect description of full dark matter haloes and may be poor fits to individual clusters. In fact numerical simulations have shown that fitting models can lead to masses underestimated by ~5%-10% (Becker & Kravtsov 2011; Schrabback et al. 2016; Henson et al. 2017). To mitigate potential biases we restrict the scales at which we fit our models to 0.5 - 2 Mpc scales, where the models are reasonable descriptions of dark matter distributions. At large radii the density models go to zero whereas large scale structure surrounding the cluster contributes to the shear signal in the real Universe. Estimated masses will be biased due to this mismatch, unless the fit is restricted to intermediate scales (Corless & King 2007; Becker & Kravtsov 2011; Rasia et al. 2012). At small radii the shears can become very large for which our shape measurement algorithm was not calibrated, so we also exclude these scales. By excluding the cluster core we also limit the impact of miscentring in

our mass estimates (see Section 4.5.4).

Uncorrelated structures along the line of sight do not bias the lensing signal (Hoekstra 2001), but introduce an additional uncertainty that cannot be distinguished from the cluster signal. We use the predictions from Hoekstra et al. (2011a) to incorporate the effect of distant large scale structure into the errorbars on our weak lensing masses.

4.5.1 Singular isothermal sphere

The simplest profile to fit to the tangential shear profile is the projected singular isothermal sphere (SIS)

$$\gamma_{\rm t}(R) = \frac{R_{\rm E}}{2R}. \tag{4.8}$$

The SIS profile is useful to consider because it can be directly linked to dynamical estimates of the cluster. The Einstein radius $R_{\rm E}$ in radians is related to the velocity dispersion of the cluster projected along the line of sight σ_v, assuming isotropic orbits and spherical symmetry,

$$R_{\rm E} = 4\pi\langle\beta\rangle\frac{\sigma_v^2}{c^2}, \tag{4.9}$$

where c is the speed of light. For the MENeaCS clusters Sifón et al. (2015) compiled a catalogue of cluster members and computed the velocity dispersions from spectroscopic redshifts. We fit the SIS model to our weak lensing data to compare with the dynamical velocity dispersions.

The convergence κ for a SIS is given by the same expression as the shear and we fit the reduced shear $g = \gamma/(1-\kappa)$ (corrected for using Equation 4.5) to our measured reduced shears. The best fit Einstein radii and resulting velocity dispersions are listed for all clusters in Table 4.2. For the radial range 0.5-2 Mpc the convergence is negligible and we note that instead fitting the reduced shear directly with Equation 4.8 would alter the Einstein radii by only 0.5%.

The comparison between the velocity dispersions from the SIS fit to the dynamical velocity dispersions from Sifón et al. (2015) is shown in Figure 4.4. Black points show results for the MENeaCS clusters and gray points show CCCP clusters from H15. The MENeaCS clusters have on average lower velocity dispersions (and thus lower masses according to the virial theorem) than the CCCP clusters. The volume from which the local MENeaCS clusters are drawn is small compared to the volume for the CCCP clusters. As the mass function decreases rapidly for high masses, and both surveys target the most massive clusters in their respective volumes, we expect on average lower masses for MENeaCS clusters.

To fit the data points with errorbars on both axes, we represent each data point as an elliptical Gaussian distribution where the width is set by the errorbars and we randomly sample from the distribution to recreate our measurements many times. For each mock measurement we fit a straight line with only a slope and no offset. The analysis shows that there is decent agreement between the velocity dispersion estimates for the MENeaCS clusters. On average the weak lensing estimates are roughly 2σ higher than the dynamical estimates, where *sigma* was determined from the 16th and 84th percentiles of the distribution. The full sample of MENeaCS and CCCP are consistent with a one-to-one relation. We perform a formal Kolmogorov-Smirnov test on the difference between the two velocity dispersion estimates for the two clusters samples. The p-value is 0.18, so we can be confident that the two samples are drawn from the same underlying distribution.

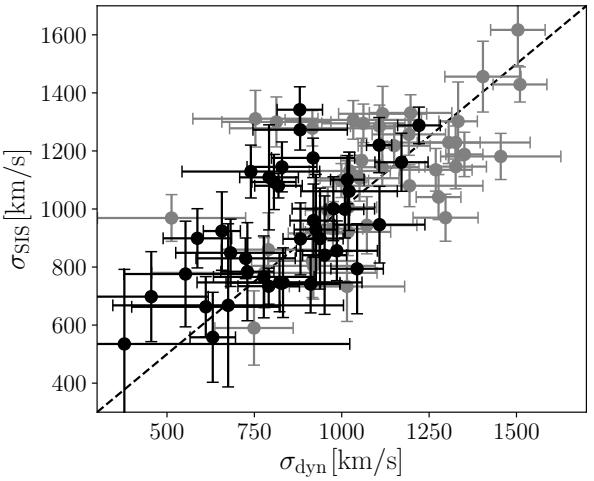

Figure 4.4: Velocity dispersion σ from SIS fit to the weak lensing against the dynamical velocity dispersion taken from Sifón et al. (2015). Black points show our results and gray points show the same for clusters in the CCCP sample of H15. The dashed line shows a one to one relation.

4.5.2 Navarro-Frenk-White profile

An often used profile to describe dark matter haloes is the Navarro-Frenk-White (NFW) profile, which, unlike the SIS profile, is known to be a good fit to observational data (e.g. Okabe et al. 2013; Umetsu et al. 2014; Viola et al. 2015). In numerical simulations Navarro et al. (1997) found a universal profile for the density of dark matter haloes

$$\frac{\rho(r)}{\rho_0} = \frac{\delta_c(\Delta)}{(r/r_\mathrm{s})(1 + r/r_\mathrm{s})^2}, \tag{4.10}$$

where the radial shape of the profile is defined by the scale radius r_s[3]. The amplitude of the profile is set by the characteristic overdensity

$$\delta_c(\Delta) = \frac{\Delta}{3} \frac{c_\Delta^3}{\ln(1 + c_\Delta) + c_\Delta/(1 + c_\Delta)}, \tag{4.11}$$

which depends on the concentration c_Δ. For a fixed number Δ the concentration is the ratio of the radius r_Δ enclosing a sphere of density $\Delta\rho_0$ and the scale radius: $c_\Delta = r_\Delta/r_\mathrm{s}$. The mass within this region can be obtained from:

$$M_\Delta = \Delta\rho_0 \frac{4\pi}{3} r_\Delta^3. \tag{4.12}$$

The density ρ_0 is usually set to the critical density of the Universe $\rho_\mathrm{crit} = 3H(z)^2/8\pi G$ or the mean density of the Universe $\rho_\mathrm{mean} = \Omega_\mathrm{m}\rho_\mathrm{crit}$ in combination with some characteristic value for Δ. For our analysis we use the mean density $\rho_0 = \rho_\mathrm{mean}$ in Equations 4.10 and 4.12 and the overdensity factor $\Delta_\mathrm{vir} = \left(18\pi^2 + 82\Omega_\Lambda(z) - 39\Omega_\Lambda(z)^2\right)/\Omega_\mathrm{m}(z)$, where

[3]Here the scale radii r and r_s are three dimensional quantities in contrast to the two dimensional Einstein radius R_E and cluster-centric radius R.

$\Omega_\Lambda(z)$ and $\Omega_m(z)$ are the energy densities of dark energy and matter at redshift z, respectively (e.g. Coe 2010). The resulting mass estimate from the NFW profile is the virial mass M_{vir}.

We follow the definitions in Wright & Brainerd (2000) to fit a projected NFW profile to our lensing signal. We combine their expressions for γ and κ to create an NFW profile for the tangential reduced shear, again with the additional terms given in Equation 4.5. The free parameters in the NFW model are correlated and the concentration depends on redshift. In practice, the concentration is constrained using numerical dark matter simulations (e.g. Duffy et al. 2008; Dutton & Macciò 2014; Diemer & Kravtsov 2015). We follow H15 and use the mass concentration relation found by Dutton & Macciò (2014), which is in good agreement with later work by Diemer & Kravtsov (2015) for our low redshift clusters. With the addition of the mass-concentration relation, our fitting function only has the virial mass as a free parameter. We fit our corrected reduced shear signals with an NFW model and list the best fit virial masses and corresponding viral radii r_{vir} in Table 4.2. We find that taking into account the uncertainty in the masses due to distant large scale structure inflates the errorbars by ∼20%.

In Figure 4.5 we show the inverse variance weighted average shear signal multiplied by the critical surface density to account for the different lensing efficiencies of the clusters. Each individual reduced shear profile is converted to shear γ using the individual best fit mass estimates to compute κ. The best fit NFW profiles are also shown and are visually a good representation of the data. The average NFW virial mass is $8.26 \pm 0.40 \times 10^{14} M_\odot$ and is shown as the red point in the inset. If we leave the concentration as a free fit parameter we obtain $7.93 \pm 0.60 \times 10^{14} M_\odot$ (blue contours). Our data shows an average mass and concentration consistent with the results we get when using the results of Dutton & Macciò (2014).

It is instructive to compare our best fit NFW masses other available mass estimates. Rines et al. (2016) have used spectroscopic redshifts to identify caustics, which can be related to the escape velocity in the cluster potential. They provide M_{200} dynamical masses for 24 MENeaCS clusters. We convert our NFW virial masses to M_{200} using the expressions given in Hu & Kravtsov (2003)[4]. For M_{200} this amounts to equating $\rho_{mean}\ \delta_c(\Delta_{vir}) = \rho_{crit}\ \delta_c(200)$ and solving for c_{200}. The resulting M_{200} masses are listed in Table 4.2 and compared to the dynamical estimates in Figure 4.6. The 24 MENeaCS clusters are shown in black and 18 CCCP clusters are shown in gray. Simple linear regression shows that the weak lensing masses are higher than the dynamical masses by a factor of ∼20%. This discrepancy is consistent for both the MENeaCS and the CCCP sample. H15 discussed that the discrepancy could be reduced (but not removed) by excluding outliers, which were also commented upon by Rines et al. (2013). The bulk of the MENeaCS clusters have consistently higher weak lensing mass compared to the dynamical mass, making it difficult to explain the difference based on individual clusters. Moreover, we could not find discussions on the dynamical masses or dynamical states for all clusters with a large difference between the masses estimates. One of these outlying clusters, Abell 2243, is a known merging system, so that the dynamical mass might be poorly constrained. There is no satisfactory explanation for the discrepancy of the mass estimates, but we do find that the overall discrepancy is consistent for both the MENeaCS and the CCCP clusters.

[4]The conversion is not strictly necessary here as Dutton & Macciò (2014) derive a relation for $c_{200}(M_{200})$, so that it is possible to fit the NFW profile directly for M_{200}. However, the same cannot be done for M_{500}, which we shall use in Section 4.5.3, so we employ the conversion already here.

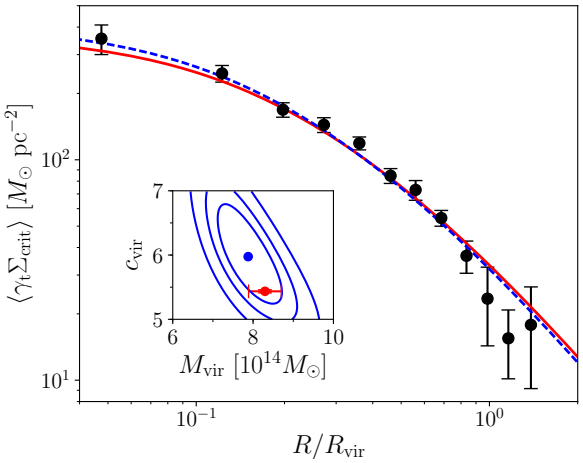

Figure 4.5: Stacked profile of the shear times critical surface density (also known as the excess surface density profile) as a function of the virial radius. Errorbars were computed using a sufficiently large number of bootstraps for each bin. The red solid line shows the best fit NFW profile using the Dutton & Macciò (2014) mass-concentration relation, and the blue dashed line shows the best fit, when leaving the concentration as a free fit parameter. The inset shows for the same colours the best fit mass and concentration and contours show the 68%, 90%, and 99% confidence intervals.

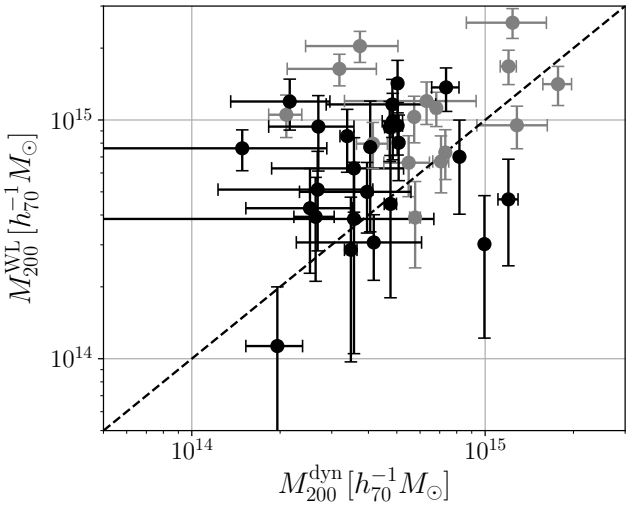

Figure 4.6: Comparison of the weak lensing masses $M_{200}^{\rm WL}$ and the dynamical masses $M_{200}^{\rm dyn}$ from Rines et al. (2016). Black points show our results and gray points show the results for CCCP clusters from H15. The dashed line shows unity slope.

4.5.3 Hydrostatic mass comparison

The *Planck* all-sky survey has produced a large catalogue of clusters detected through the SZ effect (Planck Collaboration et al. 2016c). Planck Collaboration et al. (2016b) used 439 clusters to constrain cosmological parameters by measuring the cluster mass function at different epochs. Cluster masses were computed using a scaling relation between the hydrostatic X-ray mass and the SZ observable $Y_{\rm SZ}$ (integrated Compton y-profile) based on a universal pressure profile (Arnaud et al. 2010). X-ray mass estimates can be biased because the underlying assumption of hydrostatic equilibrium is violated in galaxy clusters by bulk gas motions and non-thermal pressure support (e.g. Rasia et al. 2012), or due to uncertainties related to the calibration of X-ray observables (Mahdavi et al. 2013), and possibly by the assumption of a pressure profile. Planck Collaboration et al. (2016b) find that a bias $M_{Planck}/M_{\rm true} \equiv 1-b = 0.58\pm0.04$ is required to attain consistency between cosmological parameter constraints obtained with the cluster mass function and those obtained using primary CMB measurements (Planck Collaboration et al. 2016a). Such a low bias is not fully supported by independent mass measurements. von der Linden et al. (2014b) find a bias $1-b = 0.69\pm0.07$, which is marginally consistent, but H15 find a higher value $1-b = 0.76\pm0.05({\rm stat})\pm0.06({\rm syst})$, and Smith et al. (2016) find that b is consistent with zero. However, Battaglia et al. (2016) showed that adding a correction for Eddington bias would bring the results of WtG and CCCP more in line with the required *Planck* value.

The *Planck* cluster masses are based on the Compton y-profile integrated out to a radius of r_{500}. Therefore we have computed M_{500} estimates based on the NFW profile for a direct comparison (the values are listed in column 10 in Table 4.2). In Figure 4.7 our mass estimates $M_{500}^{\rm WL}$ are shown as a function of the *Planck* masses $M_{500}^{\rm SZ}$ in black for 30 clusters in MENeaCS in common with the *Planck* catalogue and in gray we show the same for 37 CCCP clusters.

We fit a linear scaling relation between the two mass estimates accounting for errors in both mass estimates and allowing for intrinsic scatter in the hydrostatic masses. For MENeaCS we find $M_{500}^{\rm WL} = (1.03\pm0.08)M_{500}^{\rm SZ}$ with an intrinsic scatter of $29\pm10\%$. This value is notably different from the scaling relation 0.76 ± 0.05 (stat) ±0.06 (syst) found by H15. If we repeat our analysis for the CCCP clusters using the computed NFW masses and the updated *Planck* masses (Planck Collaboration et al. 2016c), we find a bias of 0.83 ± 0.06, which is still inconsistent with the results for MENeaCS. A similar difference in scaling relations between samples of clusters at different redshifts was already noted by Smith et al. (2016). They suggested a redshift dependent hydrostatic mass bias, possibly arising due to systematic errors in weak lensing measurements or departures from self-similar evolution (Andreon 2014).

Alternatively, von der Linden et al. (2014b) advocated a mass dependence in the hydrostatic bias, which was also seen in other observations by H15 and Mantz et al. (2016) (who used the WtG weak lensing measurements) and hinted at in numerical simulations of clusters. Henson et al. (2017) find that the bias in X-ray masses increases from 20% to 40% with the true cluster mass for clusters in a mass range from $\sim 10^{14} - 10^{15}h_{70}^{-1}M_\odot$. Nagai et al. (2007) find lower hydrostatic biases of $5-20\%$ for a relatively low mass sample with $\langle M_{500}\rangle = 4.14h_{70}^{-1}M_\odot$, whereas Rasia et al. (2012) examine a sample of more massive clusters and find a higher range of biases around $\sim 25-35\%$. As the CCCP clusters are more massive than the MENeaCS clusters, such a mass dependent hydrostatic mass bias could explain the difference in the scaling relations.

We take advantage of the large range in masses in the combined sample of CCCP

and MENeaCS to investigate a potential mass dependence of the hydrostatic bias. For consistency we use the masses from NFW fits for the CCCP clusters, but H15 showed that the mass estimates are consistent. We fit the combined sample with a linear relation, finding $M_{500}^{\rm WL} = (0.90 \pm 0.05) M_{500}^{\rm SZ}$ and an intrinsic scatter of $34 \pm 5\%$. To allow for a mass dependence we fit a power law and find

$$\frac{M_{500}^{\rm SZ}}{10^{15} M_\odot} = (0.84 \pm 0.07) \left(\frac{M_{500}^{\rm WL}}{10^{15} M_\odot} \right)^{(0.82 \pm 0.08)} \tag{4.13}$$

and an intrinsic scatter of $29 \pm 6\%$. Both lines are shown in Figure 4.7. The power law fit clearly favors a power different than one, indicating that the data prefer mass evolution. This is also backed up by the slightly lower intrinsic scatter found for the power law. Both the amplitude 0.84 ± 0.07 and the slope of the power law 0.82 ± 0.08 are consistent with the results from H15: 0.76 ± 0.04 and 0.64 ± 0.17, respectively. The slope is also consistent with the WtG results of $0.68^{+0.15}_{-0.11}$ (von der Linden et al. 2014b) and 0.73 ± 0.02 (Mantz et al. 2016), but, as for CCCP, this is mainly due to the large errorbars.

A potential caveat in our analysis is the use of NFW profiles. Although the NFW profile is a good description for a stack of clusters, simulations suggest they are biased low (e.g. Bahé et al. 2012). Gravitational lensing measures the density contrast and the NFW profile might be biased for merging systems (see e.g. Hoekstra et al. 2000 for how substructure affects the mass estimates). We find several known merging systems as outliers in the population and omitting them in the analysis reduces the slope and the power for the power law by $\sim 0.5\sigma$. An alternative approach would be to use the aperture mass (Fahlman et al. 1994; Clowe et al. 1998), which estimates the mass inside an aperture and should be more robust against the state of the matter distribution. H15 showed that aperture masses were consistent with NFW masses and in future work we shall verify this for the MENeaCS clusters. In addition, a more careful analysis should incorporate the effect of Eddington bias, the importance of which has been shown by Battaglia et al. (2016). At low masses, not all MENeaCS have measurements of $M_{500}^{\rm SZ}$ and such selection effects could be mistaken for a mass dependence of the hydrostatic mass bias.

4.5.4 Systematic error budget

A large part of this work has been devoted to corrections for systematic effects. Here we review their impact on our mass estimates.

In our analysis we have assumed that the centre of the cluster is given by the location of the BCG. If the BCG is not in the bottom of the gravitational potential the NFW profile is miscentred and the mass estimates will be biased. However, the red line in Figure 4 in Hoekstra et al. (2011b) shows that for our conservative choice of 0.5 Mpc as the lower limit of the fit range the bias is only ~5% if the BCG is 100 kpc from the true cluster centre. Mahdavi et al. (2013) and Bildfell (2013) looked at the distance between the BCG location and the peak in the X-ray surface brightness, and for small distances they are a good indicator for the centre of the gravitational potential of the cluster (George et al. 2012). They found that most of the CCCP clusters have a BCG offset smaller than 100 kpc. If we assume a similar distribution for the MENeaCS clusters, we expect a bias of much less than 5% in our average cluster mass.

The uncertainty in the shear estimates for our pipeline was tested by H15 and they found an accuracy of ~1%. They conservatively assign a 2% uncertainty in their

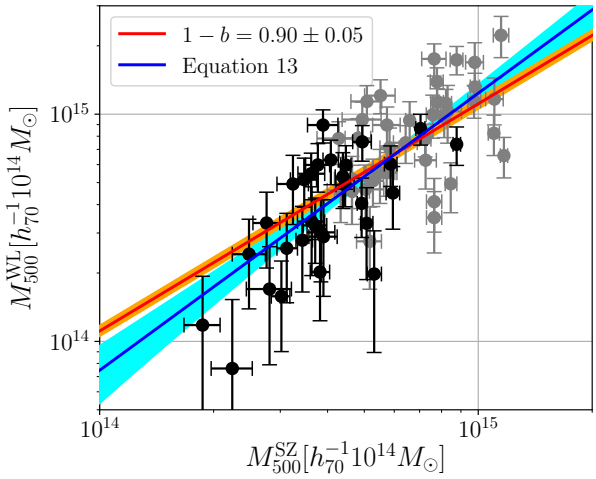

Figure 4.7: Comparison of the weak lensing masses M_{500} and the SZ masses from *Planck*. Black points show our results and gray points show the same for clusters in the CCCP sample of H15. The red line shows the best fit scaling relation using a constant hydrostatic mass bias and the scatter is shown as the orange band. The blue line and cyan shaded region show the same for the best power law fit.

analysis and we do the same. Thanks to a new high-fidelity photometric redshift catalogue, the uncertainty in our source redshift distribution is $\lesssim$1.5%, much better than the 4.2% uncertainty found for CCCP. The boost corrections applied to our tangential shear profiles are accurate to ~1%. We find that not applying the boost corrections, contamination of cluster members in the source sample would reduce our mass estimates by ~10%. This highlights the benefit of MENeaCS as H15 found for the same fit range a ~20% effect for the higher redshift CCCP clusters. These sources of errors are uncorrelated and we add them quadraticaly to find a systematic error of 2.7%. The conservatively estimated 2% uncertainty in the shear measurement is the dominant source of error. A more cavalier view would state that the uncertainties in the photometric redshifts and the shear measurement are comparable.

The overall error in our analysis of ~3% is remarkably low, despite the lack of reliable photometric redshifts for individual galaxies. This deficiency is less severe for the low redshift MENeaCS clusters and trading off multi-wavelength information against number of observed clusters has proven worth-while. We note that if the MENeaCS observations had been deeper, the available photometric redshift catalogues would not have sufficient depth to cover our source population. For weak lensing analyses of clusters at much higher redshifts multi-wavelength observations will be necessary.

4.6 Conclusions

Cluster counts have the potential to put tight constraints on cosmological parameters, if large numbers of clusters with accurate mass estimates are observed. The large survey area of cosmic microwave background experiments provides a large sample

(1)	(2) cluster	(3) R_E[arcsec]	(4) σ_{SIS} [km/s]	(5) r_{vir} [h_{70}^{-1} Mpc]	(6) M_{vir} [$10^{14} h_{70}^{-1} M_\odot$]
1	A7	19.0 ± 3.6	959 ± 92	2.86 ± 0.28	7.97 ± 2.34
2	A21	13.7 ± 2.5	803 ± 73	2.44 ± 0.22	4.85 ± 1.29
3	A85	24.6 ± 4.9	1006 ± 100	3.20 ± 0.33	10.17 ± 3.17
4	A119	20.4 ± 5.7	901 ± 126	2.82 ± 0.42	6.87 ± 3.04
5	A133	13.1 ± 2.2	737 ± 63	2.30 ± 0.19	3.78 ± 0.96
6	A646	12.0 ± 5.2	791 ± 172	2.33 ± 0.50	4.48 ± 2.89
7	A655	16.0 ± 6.2	909 ± 177	2.71 ± 0.52	7.05 ± 4.06
8	A754	30.0 ± 4.5	1111 ± 84	3.57 ± 0.27	14.07 ± 3.16
9	A780	13.6 ± 3.7	749 ± 103	2.33 ± 0.31	3.92 ± 1.56
10	A795	35.0 ± 4.3	1367 ± 85	4.02 ± 0.27	23.21 ± 4.61
11	A961	25.6 ± 4.2	1146 ± 95	3.40 ± 0.29	13.81 ± 3.52
12	A990	30.6 ± 3.6	1295 ± 76	3.76 ± 0.24	19.36 ± 3.68
13	A1033	24.3 ± 8.2	1121 ± 190	3.28 ± 0.59	12.39 ± 6.67
14	A1068	16.9 ± 4.9	952 ± 138	2.74 ± 0.41	7.37 ± 3.30
15	A1132	26.7 ± 3.2	1194 ± 72	3.49 ± 0.23	15.27 ± 3.01
16	A1285	21.0 ± 4.6	1013 ± 112	3.08 ± 0.34	9.89 ± 3.33
17	A1348	11.5 ± 3.8	763 ± 125	2.27 ± 0.35	4.04 ± 1.87
18	A1361	16.4 ± 3.8	906 ± 105	2.68 ± 0.31	6.69 ± 2.35
19	A1413	21.3 ± 5.6	1076 ± 140	3.14 ± 0.42	11.20 ± 4.47
20	A1650	26.2 ± 2.1	1091 ± 43	3.35 ± 0.14	12.33 ± 1.54
21	A1651	19.2 ± 7.9	939 ± 193	2.92 ± 0.59	8.16 ± 4.98
22	A1781	6.8 ± 6.6	536 ± 259	1.74 ± 0.73	1.65 ± 2.08
23	A1795	31.7 ± 4.9	1156 ± 89	3.65 ± 0.29	15.27 ± 3.66
24	A1927	14.9 ± 2.6	836 ± 71	2.54 ± 0.22	5.43 ± 1.39
25	A1991	14.5 ± 6.9	779 ± 184	2.43 ± 0.57	4.49 ± 3.17
26	A2029	38.6 ± 3.8	1308 ± 64	4.12 ± 0.20	22.56 ± 3.23
27	A2033	12.3 ± 3.3	744 ± 101	2.27 ± 0.30	3.82 ± 1.49
28	A2050	14.9 ± 3.6	865 ± 105	2.58 ± 0.31	5.95 ± 2.16
29	A2055	11.8 ± 3.8	752 ± 122	2.28 ± 0.37	3.99 ± 1.92
30	A2064	9.1 ± 7.8	668 ± 286	2.02 ± 0.79	2.83 ± 3.33
31	A2065	31.6 ± 5.5	1175 ± 102	3.69 ± 0.33	16.13 ± 4.39
32	A2069	12.9 ± 5.1	800 ± 157	2.40 ± 0.46	4.75 ± 2.74
33	A2142	33.2 ± 5.2	1240 ± 96	3.86 ± 0.29	19.00 ± 4.34
34	A2420	27.0 ± 6.7	1111 ± 136	3.45 ± 0.43	13.45 ± 5.04
35	A2426	20.1 ± 7.4	979 ± 181	2.92 ± 0.56	8.32 ± 4.82
36	A2440	26.3 ± 4.7	1107 ± 98	3.40 ± 0.30	13.01 ± 3.48
37	A2443	28.4 ± 5.7	1178 ± 118	3.55 ± 0.37	15.20 ± 4.80
38	A2495	7.0 ± 3.9	560 ± 156	1.75 ± 0.44	1.75 ± 1.32
39	A2597	16.1 ± 4.4	855 ± 118	2.62 ± 0.36	5.87 ± 2.43
40	A2627	9.7 ± 2.8	706 ± 101	2.10 ± 0.30	3.24 ± 1.40
41	A2670	21.0 ± 5.7	965 ± 130	2.94 ± 0.41	8.20 ± 3.45
42	A2703	17.6 ± 5.2	933 ± 138	2.78 ± 0.42	7.43 ± 3.33
43	MKW3S	11.1 ± 3.5	665 ± 105	2.09 ± 0.32	2.77 ± 1.27
44	RXJ0132	7.9 ± 3.4	663 ± 142	1.95 ± 0.40	2.71 ± 1.66
45	RXJ0736	9.8 ± 4.4	703 ± 157	2.10 ± 0.46	3.23 ± 2.11
46	RXJ2344	17.2 ± 5.0	878 ± 126	2.68 ± 0.39	6.27 ± 2.74
47	ZWCL1023	10.9 ± 4.0	772 ± 143	2.26 ± 0.41	4.17 ± 2.25
48	ZWCL1215	16.3 ± 7.9	848 ± 207	2.67 ± 0.63	6.13 ± 4.37

(1)	(2) cluster	(7) r_{200} [h_{70}^{-1} Mpc]	(8) M_{200} [h_{70}^{-1} Mpc]	(9) r_{500} [h_{70}^{-1} Mpc]	(10) M_{500} [h_{70}^{-1} Mpc]
1	A7	1.58 ± 0.16	5.00 ± 1.64	1.01 ± 0.10	3.24 ± 1.07
2	A21	1.35 ± 0.13	3.07 ± 0.94	0.86 ± 0.08	2.02 ± 0.62
3	A85	1.74 ± 0.19	6.27 ± 2.16	1.11 ± 0.12	4.05 ± 1.40
4	A119	1.53 ± 0.23	4.27 ± 1.99	0.98 ± 0.15	2.79 ± 1.30
5	A133	1.26 ± 0.11	2.39 ± 0.70	0.81 ± 0.07	1.58 ± 0.46
6	A646	1.30 ± 0.28	2.86 ± 1.89	0.84 ± 0.18	1.88 ± 1.24
7	A655	1.51 ± 0.30	4.45 ± 2.65	0.97 ± 0.19	2.89 ± 1.72
8	A754	1.93 ± 0.16	8.61 ± 2.31	1.23 ± 0.10	5.52 ± 1.48
9	A780	1.27 ± 0.17	2.48 ± 1.05	0.82 ± 0.11	1.64 ± 0.70
10	A795	2.22 ± 0.17	14.24 ± 3.53	1.40 ± 0.11	8.96 ± 2.22
11	A961	1.88 ± 0.17	8.56 ± 2.52	1.19 ± 0.11	5.47 ± 1.61
12	A990	2.09 ± 0.15	11.95 ± 2.88	1.32 ± 0.10	7.56 ± 1.82
13	A1033	1.82 ± 0.33	7.70 ± 4.30	1.15 ± 0.21	4.93 ± 2.76
14	A1068	1.53 ± 0.23	4.65 ± 2.20	0.98 ± 0.15	3.02 ± 1.42
15	A1132	1.94 ± 0.14	9.47 ± 2.34	1.23 ± 0.09	6.03 ± 1.49
16	A1285	1.70 ± 0.20	6.16 ± 2.27	1.08 ± 0.13	3.98 ± 1.46
17	A1348	1.26 ± 0.20	2.58 ± 1.25	0.81 ± 0.13	1.70 ± 0.83
18	A1361	1.49 ± 0.18	4.22 ± 1.61	0.95 ± 0.12	2.75 ± 1.05
19	A1413	1.75 ± 0.24	7.01 ± 2.98	1.11 ± 0.15	4.50 ± 1.91
20	A1650	1.83 ± 0.10	7.61 ± 1.48	1.17 ± 0.06	4.89 ± 0.95
21	A1651	1.60 ± 0.33	5.09 ± 3.20	1.02 ± 0.21	3.31 ± 2.07
22	A1781	0.96 ± 0.41	1.06 ± 1.35	0.62 ± 0.26	0.72 ± 0.91
23	A1795	1.98 ± 0.17	9.33 ± 2.63	1.26 ± 0.11	5.97 ± 1.68
24	A1927	1.40 ± 0.13	3.43 ± 1.01	0.90 ± 0.08	2.25 ± 0.66
25	A1991	1.33 ± 0.32	2.83 ± 2.04	0.85 ± 0.20	1.87 ± 1.35
26	A2029	2.24 ± 0.13	13.69 ± 2.83	1.41 ± 0.08	8.65 ± 1.79
27	A2033	1.25 ± 0.17	2.43 ± 1.01	0.81 ± 0.11	1.60 ± 0.67
28	A2050	1.43 ± 0.18	3.76 ± 1.48	0.92 ± 0.12	2.46 ± 0.96
29	A2055	1.27 ± 0.21	2.54 ± 1.28	0.81 ± 0.13	1.68 ± 0.84
30	A2064	1.13 ± 0.44	1.82 ± 2.15	0.73 ± 0.29	1.21 ± 1.43
31	A2065	2.01 ± 0.20	9.87 ± 3.06	1.27 ± 0.12	6.29 ± 1.95
32	A2069	1.33 ± 0.26	3.02 ± 1.80	0.85 ± 0.17	1.98 ± 1.18
33	A2142	2.11 ± 0.18	11.62 ± 3.17	1.33 ± 0.11	7.37 ± 2.01
34	A2420	1.89 ± 0.24	8.29 ± 3.34	1.20 ± 0.16	5.31 ± 2.14
35	A2426	1.61 ± 0.32	5.20 ± 3.11	1.03 ± 0.20	3.37 ± 2.02
36	A2440	1.86 ± 0.18	8.03 ± 2.46	1.18 ± 0.11	5.15 ± 1.58
37	A2443	1.95 ± 0.22	9.38 ± 3.27	1.24 ± 0.14	5.98 ± 2.08
38	A2495	0.97 ± 0.25	1.13 ± 0.87	0.63 ± 0.16	0.76 ± 0.59
39	A2597	1.44 ± 0.21	3.69 ± 1.62	0.92 ± 0.13	2.42 ± 1.06
40	A2627	1.17 ± 0.17	2.08 ± 0.95	0.75 ± 0.11	1.38 ± 0.63
41	A2670	1.61 ± 0.23	5.11 ± 2.28	1.03 ± 0.15	3.32 ± 1.48
42	A2703	1.54 ± 0.24	4.67 ± 2.21	0.98 ± 0.15	3.03 ± 1.43
43	MKW3S	1.14 ± 0.18	1.76 ± 0.85	0.73 ± 0.11	1.18 ± 0.57
44	RXJ0132	1.10 ± 0.23	1.75 ± 1.10	0.71 ± 0.15	1.16 ± 0.73
45	RXJ0736	1.18 ± 0.26	2.07 ± 1.39	0.76 ± 0.17	1.37 ± 0.92
46	RXJ2344	1.47 ± 0.22	3.93 ± 1.82	0.94 ± 0.14	2.57 ± 1.19
47	ZWCL1023	1.27 ± 0.23	2.67 ± 1.49	0.81 ± 0.15	1.76 ± 0.98
48	ZWCL1215	1.47 ± 0.35	3.85 ± 2.80	0.94 ± 0.22	2.52 ± 1.83

Table 4.2: Physical properties measured from the weak lensing signal of the MENeaCS clusters. (2) cluster name; (3) Einstein radius from the best fit SIS profile; (4) velocity dispersion from the best fit SIS profile; (5) & (7) & (9) Radius of a sphere where the cluster is overdense by a factor Δ compared to the mean (for column 5) or critical (for columns 7 and 9) density of the Universe; (6) & (8) & (10) Mass enclosed within the radius R_Δ.

of clusters, whose mass can be efficiently determined from scaling relations of cluster observables. Weak gravitational lensing can produce unbiased mass estimates of galaxy clusters, such that scaling relations can be calibrated. However, projection effects of overdensities along the line of sight to the cluster introduce a large uncertainty in the measurement, so that robust calibration requires large samples of clusters.

The Multi Epoch Nearby Cluster Survey (MENeaCS) provides high quality optical imaging data in the g and r filters observed using the Canada-France-Hawaii Telescope (CFHT) for a sample of 58 galaxy clusters. We performed a thorough weak lensing analysis on 48 clusters in this sample, excluding some of the clusters because of their very high Galactic extinction, which prevented us from establishing a robust correction for contamination by cluster members. Our shape measurement pipeline was extensively tested in Hoekstra et al. (2015) and this gives us confidence that our systematic uncertainty in the shear estimates is $\sim 2\%$.

The MENeaCS observations lack the colour information for reliable photometric redshifts and we rigorously check and correct for the uncertainties this introduces into the lensing analysis. First, the redshift distribution for the background sources in our data is approximated by the galaxy population in the COSMOS field, for which redshift information accurate to 1% is available. We consistently apply the lensing quality cuts to our photometric redshift distribution to avoid introducing biases from selection effects. To assess how representative the redshift distribution in the COSMOS field is, we use additional observations of four CFHT Legacy Survey Deep fields and find that the redshift uncertainty for our source population is at most 1.5%.

Second, without redshifts for individual sources we cannot discriminate between cluster members and field galaxies. We statistically correct for the contamination of our source sample by applying a boost correction to the shear signal. The lowest redshift clusters fill the entire field of view, so that the weight density in the cluster fields cannot be compared to the weight density of source galaxies. To overcome this issue, we used additional deep observations of blank parts of the sky from the CFHT archive to compute the average weight density for field galaxies. We determine the expected field galaxy weight density as a function of the seeing, depth of the observations and the Galactic extinction and find only a marginal uncertainty of 1% on our best fit. The intrinsic scatter in the weight density of around ~6% is smaller than the statistical uncertainty in the shear estimates. The final boost corrections have a residual contamination of cluster members into source sample of $\lesssim 1\%$.

The radial profiles of the boost corrected tangential shear were fit with parametric models to estimate physical properties of the clusters. Velocity dispersions from an SIS fit and masses from an NFW fit agree reasonably well with estimates based on dynamics of cluster members. The CCCP and MENeaCS samples were observed under the same conditions with the same telescope and analysed with the same pipeline. We check that the two samples are similar and find no evidence for a systematic difference.

Finally, we perform an analysis to compute a scaling relation between weak lensing masses and hydrostatic masses estimates from Planck Collaboration et al. (2016c), for 30 clusters in common between MENeaCS and *Planck*, which results in a bias of $1 - b = 1.03 \pm 0.08(\mathrm{stat}) \pm 0.03(\mathrm{syst})$. This value is high compared what was found for the CCCP and Weighing the Giants cluster samples, but in agreement with results of LoCuSS. The variation in hydrostatic estimates hints at an evolution of the hydrostatic bias with mass, as has been found in numerical simulations of clusters. We combine the CCCP and MENeaCS samples to extend the mass range of the clusters and find that a power law is a better fit to the data than a constant hydrostatic bias. In future

work we shall use another mass estimator to check the effect of structure in the cluster and incorporate a careful treatment of Eddington bias. This will help to verify the mass dependence of the hydrostatic mass bias. It is unclear what the impact of such a mass dependence is for the tension between the cosmological parameters estimated from primary CMB and cluster counts.

Acknowledgements

We thank Anja Von der Linden for helpful comments.

This work is based on observations obtained with MegaPrime/MegaCam, a joint project of CFHT and CEA/IRFU, at the Canada-France-Hawaii Telescope (CFHT) which is operated by the National Research Council (NRC) of Canada, the Institut National des Science de l'Univers of the Centre National de la Recherche Scientifique (CNRS) of France, and the University of Hawaii. This work is based in part on data products produced at Terapix available at the Canadian Astronomy Data Centre as part of the Canada-France-Hawaii Telescope Legacy Survey, a collaborative project of NRC and CNRS.

RH, CS, HH acknowledge support from the European Research Council FP7 grant number 279396.

Bibliography

Allen S. W., Evrard A. E., Mantz A. B., 2011, ARA&A, 49, 409

Amodeo S., et al., 2017, preprint, (`arXiv:1704.07891`)

Andreon S., 2014, A&A, 570, L10

Applegate D. E., et al., 2014, MNRAS, 439, 48

Arnaud M., Pratt G. W., Piffaretti R., Böhringer H., Croston J. H., Pointecouteau E., 2010, A&A, 517, A92

Bahé Y. M., McCarthy I. G., King L. J., 2012, MNRAS, 421, 1073

Bartelmann M., Schneider P., 2001, Phys. Rep., 340, 291

Battaglia N., Bond J. R., Pfrommer C., Sievers J. L., 2012, ApJ, 758, 74

Battaglia N., et al., 2016, JCAP, 8, 013

Becker M. R., Kravtsov A. V., 2011, ApJ, 740, 25

Bertin E., 2006, in Gabriel C., Arviset C., Ponz D., Enrique S., eds, Astronomical Society of the Pacific Conference Series Vol. 351, Astronomical Data Analysis Software and Systems XV. p. 112

Bertin E., 2010, SWarp: Resampling and Co-adding FITS Images Together, Astrophysics Source Code Library (ascl:1010.068)

Bildfell C. J., 2013, PhD thesis, University of Victoria (Canada

Bildfell C., Hoekstra H., Babul A., Mahdavi A., 2008, MNRAS, 389, 1637

Bleem L. E., et al., 2015, ApJS, 216, 27

Bocquet S., et al., 2015, ApJ, 799, 214

Böhringer H., et al., 2004, A&A, 425, 367

Borgani S., Guzzo L., 2001, Nature, 409, 39

Clowe D., Luppino G. A., Kaiser N., Henry J. P., Gioia I. M., 1998, ApJL, 497, L61

Coe D., 2010, preprint, (arXiv:1005.0411)

Corless V. L., King L. J., 2007, MNRAS, 380, 149

Coupon J., et al., 2009, A&A, 500, 981

Diemer B., Kravtsov A. V., 2015, ApJ, 799, 108

Duffy A. R., Schaye J., Kay S. T., Dalla Vecchia C., 2008, MNRAS, 390, L64

Dutton A. A., Macciò A. V., 2014, MNRAS, 441, 3359

Fahlman G., Kaiser N., Squires G., Woods D., 1994, ApJ, 437, 56

George M. R., et al., 2012, ApJ, 757, 2

Gladders M. D., Yee H. K. C., 2005, ApJS, 157, 1

Graham M. L., et al., 2012, ApJ, 753, 68

Gruen D., Brimioulle F., 2016, preprint, (arXiv:1610.01160)

Gwyn S. D. J., 2008, PASP, 120, 212

Hasselfield M., et al., 2013, JCAP, 7, 008

Henson M. A., Barnes D. J., Kay S. T., McCarthy I. G., Schaye J., 2017, MNRAS, 465, 3361

Hoekstra H., 2001, A&A, 370, 743

Hoekstra H., Franx M., Kuijken K., 2000, ApJ, 532, 88

Hoekstra H., Hartlap J., Hilbert S., van Uitert E., 2011a, MNRAS, 412, 2095

Hoekstra H., Donahue M., Conselice C. J., McNamara B. R., Voit G. M., 2011b, ApJ, 726, 48

Hoekstra H., Mahdavi A., Babul A., Bildfell C., 2012, MNRAS, 427, 1298

Hoekstra H., Herbonnet R., Muzzin A., Babul A., Mahdavi A., Viola M., Cacciato M., 2015, MNRAS, 449, 685

Hu W., Kravtsov A. V., 2003, ApJ, 584, 702

Jee M. J., et al., 2011, ApJ, 737, 59

Kaiser N., Squires G., Broadhurst T., 1995, ApJ, 449, 460

Kettula K., et al., 2015, MNRAS, 451, 1460

Laigle C., et al., 2016, ApJS, 224, 24

Leauthaud A., et al., 2016, preprint, (arXiv:1611.08606)

Magnier E. A., Cuillandre J.-C., 2004, PASP, 116, 449

Mahdavi A., Hoekstra H., Babul A., Bildfell C., Jeltema T., Henry J. P., 2013, ApJ, 767, 116

Mantz A., Allen S. W., Ebeling H., Rapetti D., Drlica-Wagner A., 2010, MNRAS, 406, 1773

Mantz A. B., et al., 2015, MNRAS, 446, 2205

Mantz A. B., et al., 2016, MNRAS, 463, 3582

Mellier Y., 1999, ARA&A, 37, 127

Meneghetti M., Rasia E., Merten J., Bellagamba F., Ettori S., Mazzotta P., Dolag K., Marri S., 2010, A&A, 514, A93

Nagai D., Vikhlinin A., Kravtsov A. V., 2007, ApJ, 655, 98

Navarro J. F., Frenk C. S., White S. D. M., 1997, ApJ, 490, 493

Okabe N., Smith G. P., 2016, MNRAS, 461, 3794

Okabe N., Smith G. P., Umetsu K., Takada M., Futamase T., 2013, ApJL, 769, L35

Peng C. Y., Ho L. C., Impey C. D., Rix H.-W., 2002, AJ, 124, 266

Penna-Lima M., Bartlett J. G., Rozo E., Melin J.-B., Merten J., Evrard A. E., Postman M., Rykoff E., 2016, preprint, (arXiv:1608.05356)

Planck Collaboration et al., 2014, A&A, 571, A20

Planck Collaboration et al., 2016a, A&A, 594, A13

Planck Collaboration et al., 2016b, A&A, 594, A24

Planck Collaboration et al., 2016c, A&A, 594, A27

Rasia E., et al., 2012, New Journal of Physics, 14, 055018

Rines K., Geller M. J., Diaferio A., Kurtz M. J., 2013, ApJ, 767, 15

Rines K. J., Geller M. J., Diaferio A., Hwang H. S., 2016, ApJ, 819, 63

Rowe B. T. P., et al., 2015, Astronomy and Computing, 10, 121

Ruel J., et al., 2014, ApJ, 792, 45

Rykoff E. S., et al., 2016, ApJS, 224, 1

Sand D. J., et al., 2011, ApJ, 729, 142

Sand D. J., et al., 2012, ApJ, 746, 163

Schlafly E. F., Finkbeiner D. P., 2011, ApJ, 737, 103

Schlegel D. J., Finkbeiner D. P., Davis M., 1998, ApJ, 500, 525

Schneider P., 2003, A&A, 408, 829

Schrabback T., et al., 2016, preprint, (arXiv:1611.03866)

Sereno M., Covone G., Izzo L., Ettori S., Coupon J., Lieu M., 2017, preprint, (arXiv:1703.06886)

Sifón C., Hoekstra H., Cacciato M., Viola M., Köhlinger F., van der Burg R. F. J., Sand D. J., Graham M. L., 2015, A&A, 575, A48

Sifón C., et al., 2016, MNRAS, 461, 248

Smith G. P., et al., 2016, MNRAS, 456, L74

Sunyaev R. A., Zeldovich Y. B., 1972, Comments on Astrophysics and Space Physics, 4, 173

Umetsu K., et al., 2014, ApJ, 795, 163

Vikhlinin A., et al., 2009a, ApJ, 692, 1033

Vikhlinin A., et al., 2009b, ApJ, 692, 1060

Viola M., et al., 2015, MNRAS, 452, 3529

Wright C. O., Brainerd T. G., 2000, ApJ, 534, 34

de Haan T., et al., 2016, ApJ, 832, 95

von der Linden A., et al., 2014a, MNRAS, 439, 2

von der Linden A., et al., 2014b, MNRAS, 443, 1973

4.A Blank field counts

The lack of deep multi-band data for galaxies in the MENeaCS observations prevents us from identifying cluster members. As they are unlensed and have random orientations these galaxies will dilute the shear signal and thus need to be corrected for. We correct for this contamination using a boost correction, for which we need to model the excess of galaxies in the cluster compared to the field as a function of cluster-centric radius. This approach was also used by H15, who used the observations beyond 4 Mpc from the cluster center to estimate the background level for the targets observed with MegaCam. However, the MENeaCS clusters are at much lower redshift, and for many targets the data do not extend that far out. Therefore, we follow a different approach to determine the expected background level.

We searched the CFHT MegaPipe (Gwyn 2008) archive for co-added r-band data with a total integration $T_{\rm exp} > 3600$s and image quality better than $0\farcs9$ of pointings that appeared to be blank fields (i.e. not targeting clusters). This query resulted in 46 suitable unique targets, but upon closer inspection five fields had to be rejected because of a high noise level or because the Galactic extinction was too high. The remaining 41 fields all have an r-band Galactic extinction $A_{\rm r}$ less than 0.2 magnitude

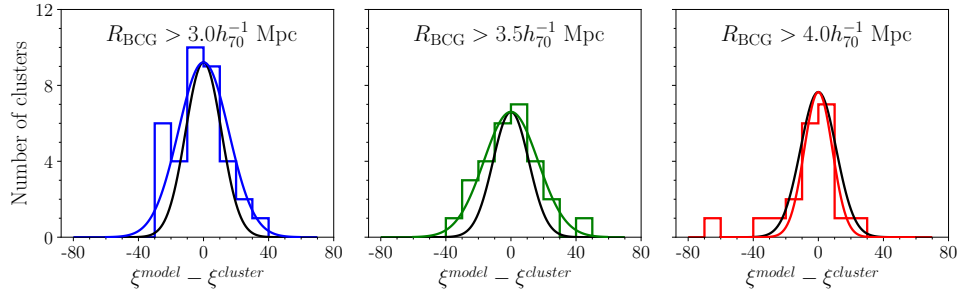

Figure 4.8: Histogram of the difference between the predicted weight density from the blank fields ξ^{model} and the weight density measured outside the cluster $\xi^{\rm cluster}$ for the highest redshift MENeaCS clusters. As the full extent of the cluster is unknown we show $\xi^{\rm cluster}$ for different areas corresponding to a radius of 3 Mpc, 3.5 Mpc and 4 Mpc from the BCG, from left to right respectively. The decreasing number of clusters shows that only the highest redshift clusters have any area available and highlights the need for the model prediction $\xi^{\rm model}$. The black curve is the same for all three panels and it shows the distribution expected from the 6% scatter around the best fit for the blank fields.

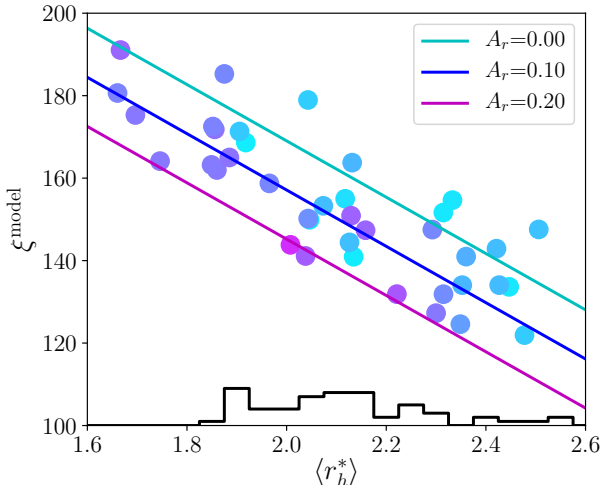

Figure 4.9: Weight density ξ as a function of the average PSF size in the image, color coded by the Galactic extinction for 41 CFHT observations homogenised to a noise rms of 1.4. Colored lines show the best fit to the data at the four different noise levels, using the same color code as the circles. The black histogram shows the distribution of PSF sizes in the MENeaCS data, covering the same range as the blank fields.

and were visually inspected to mask out obvious artifacts, leaving an effective area of approximately 33 degrees.

The noise levels vary between the images and do not match the MENeaCS data (they are typically deeper). To homogenise the data we added Gaussian noise so that all the blank fields had the same noise level. We considered four r.m.s. values σ_n =(1.2 1.4, 1.6, 1.8) to cover a range that matches most of the MENeaCS data. For the two lowest noise levels we omitted ten and two fields, respectively. The resulting images were analysed in exactly the same way as the MENeaCS data, resulting in catalogs with shape measurements and corresponding uncertainties. To quantify image quality we use the half-light radius of the PSF $r_{\rm h}^*$.

Figure 4.9 shows the resulting weight density ξ for galaxies with $20 < m_r < 24.5$ as a function of the average PSF size in the image for a noise level of 1.4. Using the blanks at all 4 different noise levels we fit a simple model to the measurements and find

$$\xi^{\rm model}(r_{\rm h}^*, \sigma_n, A_{\rm r}) = -40.6\langle r_{\rm h}^*\rangle - 68.4\sigma_{\rm n} - 122.8A_{\rm r} + 364.2, \tag{4.14}$$

where $A_{\rm r}$ is the Galactic extinction in the r-band. The color of the circles shows the extinction for each blank field and the lines show the prediction from the fit for different extinction levels in the same color scheme. For reference we also plot the distribution of PSF half-light radii found in the MENeaCS data as a black histogram in the bottom of the plot.

For the full sample we find that the r.m.s. variation in the mean weight density is 6.4%, which is smaller than the typical statistical uncertainty in the lensing signal for an individual cluster. Hence observing clusters with a single band and modelling the excess weight as a function of cluster-centric distance is an efficient way to determine masses for a large sample of clusters. Although the contamination can be largely eliminated using multi-band data, the improvement in precision is modest. On the other hand, the limited number of blank fields limits our current precision of 1% with which the average background weight density can be determined.

The blank fields have been observed with different dither patterns than the MENeaCS data. Consequently, the variations in depth will not exactly match the cluster data. To examine whether this leads to a significant systematic uncertainty, we compare the predicted weight density to the observations of high redshift clusters beyond the extent of the cluster. H15 found that the contribution from cluster members and associated structures is less than 0.5% for radii beyond 4 Mpc and we use this to define the areas in the MENeaCS observations with mostly field galaxies. Due to the low redshift of MENeaCS clusters there is very little area beyond 4 Mpc, so we vary the outer radius for a more robust comparison.

Figure 4.8 shows the distribution of the difference between the weight density in the blank field prediction and in the cluster data. For all three outer radii – 3.0 Mpc, 3.5 Mpc and 4.0 Mpc from left to right respectively – the scatter is centered around zero. The colored curves show the best fit Gaussian, which can be compared to the black curve, which shows the variation expected from the blank fields. We have fixed the centre of the Gaussian on zero, but leaving the centre as a free parameter changes little in the fit. The overall agreement between the scatter in the blank fields and the cluster outskirts is remarkably good. The scatter in all but the furthest outskirts is slightly larger than the scatter exhibited in the blank fields. The available area where $R_{\rm BCG} > 4$ Mpc is so small that the lower scatter in the cluster outskirts might be due only to low number statistics. In fact, Figure 4.2 shows little evidence for cluster members outside 2 Mpc, so that the area $R_{\rm BCG} > 3$ Mpc should also provide a clean

sample of source galaxies. Trusting the left panel in Figure 4.8, we investigate the larger scatter of the cluster data. We suspect it is caused by the limited area available in the cluster data. To check this, we re-evaluated the scatter around the blank field prediction using only part of the full blank fields. For half the area, the scatter around the best fit increased by ∼20%, which increased to ∼50% when using only a quarter of the area. As expected, the scatter increases as we decrease the size of the used area, corroborating our hypothesis for the scatter of the cluster data. This again shows that our blank field prediction for the weight density of field galaxies is a reliable tool for the normalisation of the weight density in the cluster data.